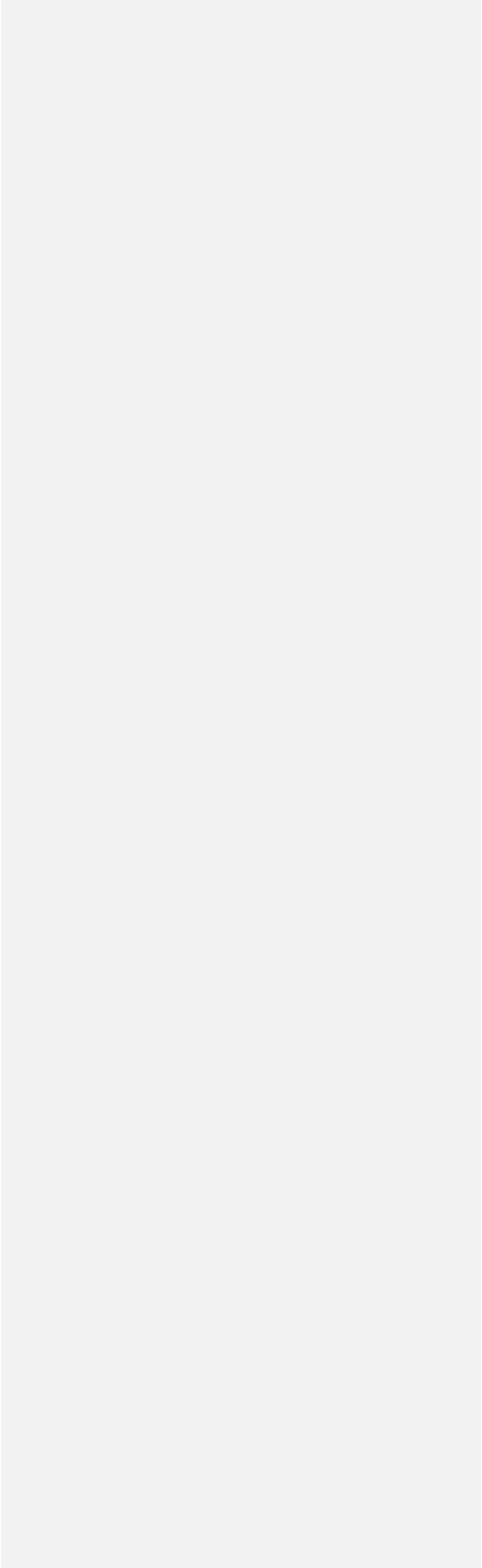


1  
2  
3  
4  
5  
6  
7  
8  
9  
10  
11  
12  
13  
14  
15  
16  
17  
18  
19  
20  
21  
22  
23  
24  
25  
26  
27  
28  
29  
30  
31  
32  
33  
34  
35  
36  
37  
38  
39  
40  
41  
42  
43

**Diapycnal mixing across the photic zone of the  
NE-Atlantic**

**by Hans van Haren, Corina P.D. Brussaard, Loes J. A.  
Gerringa, Mathijs H. van Manen, Rob Middag, Ruud  
Groenewegen**

Royal Netherlands Institute for Sea Research (NIOZ), P.O. Box 59, 1790 AB Den Burg,  
the Netherlands.  
\*e-mail: [hans.van.haren@nioz.nl](mailto:hans.van.haren@nioz.nl)



44 **Abstract.** Variable physical conditions such as vertical turbulent exchange, internal wave and  
45 mesoscale eddy action, affect the availability of light and nutrients for phytoplankton  
46 (unicellular algae) growth. It is hypothesized that changes in ocean temperature may affect  
47 ocean vertical density stratification, which may hamper vertical exchange. In order to quantify  
48 variations in physical conditions in the Northeast Atlantic Ocean, we sampled a latitudinal  
49 transect along 17±5°W between 30 and 63°N in summer. A shipborne Conductivity-  
50 Temperature-Depth CTD-instrumented package was used with a custom-made modification of  
51 the pump-inlet to minimize detrimental effects of ship motions on its data. Thorpe-scale  
52 analysis was used to establish turbulence values for the upper 500 m near the surface from 3 to  
53 6 profiles obtained in a short CTD-yoyo, 3 to 5 h after local sunrise. From south to north,  
54 temperature decreased together with stratification while turbulence values weakly increased or  
55 remained constant. Vertical turbulent nutrient fluxes ~~across the stratification did not vary were~~  
56 ~~not found to~~ significantly ~~vary~~ with stratification and latitude. This apparent lack of  
57 correspondence between turbulent mixing and temperature ~~is likely suggested to be~~ due to  
58 internal waves breaking (~~increased stratification can support more internal waves~~), ~~and~~ acting  
59 as a potential feed-back mechanism ~~because increased stratification can support more internal~~  
60 ~~waves~~. As this feed-back mechanism mediates potential physical environment changes in  
61 temperature, global surface ocean warming may not affect the vertical nutrient fluxes to a large  
62 degree. We urge for modeling testing (We urge modelers to test this deduction as it as it could  
63 imply that the future summer phytoplankton productivity in stratified oligotrophic waters would  
64 experience little alterations in nutrient input from deeper waters. we hypothesize that our  
65 findings suggest that vertical nutrient fluxes ~~nutrient availability for phytoplankton in the~~  
66 ~~euphotic surface waters may not be affected by the physical process of global warming.~~

67

68

69 **1 Introduction**

70 The physical environment is important for ocean life, including variations therein. For  
71 example, the sun stores heat in the ocean with a stable vertical density stratification as result.  
72 Generally, stratification hampers vertical turbulent exchange because of the required work  
73 against (reduced) gravity before turbulence can take effect. It thus hampers a supply of nutrients  
74 via a turbulent flux from deeper waters to the photic zone. However, stratification supports  
75 internal waves, which (i) may move near-floating particles like phytoplankton (unicellular  
76 algae) up- and down towards and away from the surface, and (ii) may induce enhanced  
77 turbulence via vertical current differences (shear) resulting in internal waves breaking (Denman  
78 and Gargett, 1983). Such changes in the physical environment are expected to affect the  
79 availability of phytoplankton growth factors such as light and nutrients.

80 Climate models predict that global warming will reduce vertical mixing in the oceans (e.g.,  
81 Sarmiento et al., 2004). Mathematical models on system stability suggest that reduced mixing  
82 may generate chaotic behaviour in phytoplankton production, thereby enhancing variability in  
83 carbon export into the ocean interior (Huisman et al., 2006). However, none of these models  
84 include potential feed-back systems like internal wave action or mesoscale eddy activity. From  
85 observations in the relatively shallow North Sea it is known that the strong seasonal temperature  
86 stratification is marginally stable, as it supports internal waves and shear to such extent that  
87 sufficient nutrients are replenished from below to sustain the late-summer [phytoplankton](#) bloom  
88 ~~in the euphotic zone near the surface that became~~ [depleted of nutrients after the spring](#)  
89 [bloom](#) (van Haren et al., 1999). This challenges the current paradigm in climate models.

90 In this paper, the objective is to resolve the effect of vertical stratification and turbulent  
91 mixing on nutrient supply to the photic zone of the open ocean. For this purpose, upper-500-  
92 m-ocean shipborne Conductivity-Temperature-Depth CTD-observations were made in  
93 association with those on dissolved inorganic nutrients during a survey along a transect in the  
94 NE-Atlantic Ocean from mid-[\(30°\)](#) to high-[\(63°\)](#) latitudes in summer. Throughout the survey,  
95 meteorological and sea-state conditions were favourable for adequate sampling and wind



123 ~~the~~the vertical gradients ~~were presented~~ for the upper 200 m ~~and both were found to~~showed  
124 ~~an~~ increase from south to north. The present observations go deeper to 500 m, also across the  
125 non-seasonal more permanent stratification. Moreover, coinciding measurements were made of  
126 the distributions of macro-nutrients and dissolved iron. This allows vertical turbulent nutrient  
127 fluxes to be computed. It leads to a hypothesis concerning a physical feed-back mechanism that  
128 may control changes in stratification.

129

## 130 **2 Materials and Methods**

131 Between 22 July and 16 August 2017, observations were made from the R/V Pelagia in the  
132 Northeast Atlantic Ocean at stations along a transect from Iceland, starting around 60°N, to the  
133 Canary Islands, ending ~~at~~around 30°N, (Fig. 1). The transect was more or less in meridional  
134 direction, with stations along 17±5°W, all in the same time zone (UTC-1 h = local time LT).  
135 Full water-depth Rosette bottle water sampling was performed at most stations.

136 Samples for dissolved inorganic macro-nutrients were filtered through 0.2 µm Acrodisc  
137 filter and stored frozen in a HDPE pony-vial (nitrate, nitrite and phosphate) or at 4°C (silicate)  
138 until analysis. Nutrients were analysed under temperature controlled conditions using a  
139 QuAatro Gas Segmented Continuous Flow Analyser. All measurements were calibrated with  
140 standards diluted in low nutrient seawater in the salinity range of the stations to ensure that  
141 analysis remained within the same ionic strength. Phosphate (PO<sub>4</sub>), nitrate plus nitrite (NO<sub>x</sub>),  
142 were measured according to Murphy and Riley (1962) and Grasshoff et al. (1983), respectively.  
143 Silicate was analysed using the procedure of Strickland and Parsons (1968).

144 Absolute and relative precision were regularly determined for reasonably high  
145 concentrations in an in-house standard. For phosphate, the standard deviation was 0.028 µM  
146 (N = 30) for a concentration of 0.9 µM; Hence the relative precision was 3.1%. For nitrate, the  
147 values were 0.14 µM (N = 30) for a concentration of 14.0 µM, so that the relative precision was  
148 1.0%. For silicate, the values were 0.09 µM (N = 15) for a concentration of 21.0 µM, so that

149 the relative precision was 0.4%. The detection limits were 0.007, 0.012 and 0.008  $\mu\text{M}$ , for  
150 phosphate, nitrate and silicate, respectively.

151 For dissolved iron samples, the ultraclean “Pristine” sampling system for trace metals was  
152 used (Rijkenberg et al., 2015). All bottles used for storage of reagents and samples were cleaned  
153 according to an intensive three step cleaning protocol described by Middag et al. (2009).  
154 Dissolved iron concentrations were measured shipboard using a Flow Injection—  
155 Chemiluminescence method with preconcentration on iminodiaceticacid (IDA) resin as  
156 described by De Baar et al. (2008) and modified by Klunder et al. (2011). In order to validate  
157 the accuracy of the system, standard reference seawater (SAFe) was measured regularly in  
158 triplicate (Johnson et al. 1997).

159 At 19 out of 32 stations a yoyo consisting of 3 to 6 casts, totaling 72 casts, of electronic  
160 CTD profiles was done to monitor the temperature-salinity variability and to establish turbulent  
161 mixing values from 5 to 500 m below the ocean surface. The yoyo casts were made  
162 consecutively and took between 1 and 2 hours per station. They were mostly obtained in the  
163 morning: at ten stations between 6 and 8 LT, at eight stations between 8 and 10 LT, and at one  
164 station in the afternoon, around noon. As the observations were made in summer, the latitudinal  
165 difference in sunrise was 1.5 h between the northernmost (earlier sunrise) and southernmost  
166 stations. This difference is taken into account and sampling times are referenced to time after  
167 local sunrise. It is assumed that the stations sampled just after sunrise more or less reflect the  
168 upper ocean conditions of (late-) nighttime cooling convection so that vertical near-  
169 homogeneity was at a maximum, and near-surface stratification at a minimum, while the late  
170 morning and afternoon stations reflected daytime stratifying near-surface conditions due to the  
171 stabilizing solar insolation.

172

### 173 **2.1 Instrumentation and modification**

174 A calibrated SeaBird 911plus CTD was used. The CTD data were sampled at a rate of 24  
175 Hz, whilst lowering the instrumental package at a speed of  $1 \text{ m s}^{-1}$ . The data were processed  
176 using the standard procedures incorporated in the SBE-software, including corrections for cell

177 thermal mass (Lueck, 1990) using the parameter setting of Mensah et al. (2009) and sensor  
178 time-alignment. All other analyses were performed using Conservative Temperature ( $\Theta$ ),  
179 absolute salinity SA and density anomalies  $\sigma_\theta$  referenced to the surface using the Gibbs  
180 SeaWater-software (IOC, SCOR, IAPSO, 2010).

181 Observations were made with the CTD upright rather than horizontal in a lead-weighted  
182 frame without water samplers to minimize artificial turbulent overturning. Variable speeds of  
183 the flow passing the temperature and conductivity sensors will cause artificial temperature and  
184 thus apparent turbulent overturning, noticeable in near-homogeneous waters such as found near  
185 the surface during nighttime convection. To eliminate variable flow speeds, a custom-made  
186 assembly with pump in- and outlet tubes and tube-ends of exactly the same diameter was  
187 mounted to the CTD as described in van Haren and Laan (2016). This reduces frictional  
188 temperature effects of typically  $\pm 0.5$  mK due to fluctuations in pump speed of  $\pm 0.5$  m s<sup>-1</sup> when  
189 standard SBE-tubing is used (Appendix A1). The effective removal of the artificial temperature  
190 effects using the custom-made assembly is demonstrated in Fig. 2, in which surface wave action  
191 via ship motion is visible in the CTD-pressure record, but not in its temperature variations  
192 record. For example, at station 32 the CTD was lowered in moderate sea state conditions with  
193 surface waves of maximum 2 m crest-trough. The surface waves are recorded by pressure  
194 variations as a result of ship motions (Fig. 2a). In the upper 40 m near the surface, the waters  
195 were near-homogeneous, with temperature variations well within  $\pm 0.5$  mK (Fig. 2b). The  $\Delta T$ -  
196 variations did not vary with the surface wave periodicity of about 10 s. No correlation is found  
197 between data in Fig. 2b and Fig. 2a. This effective removal of ship motion in CTD-temperature  
198 data is confirmed for the entire 500 m depth-range in average spectral information (Fig. 2c-e).  
199 In the power spectra, the pressure gradient  $dp/dt \sim$  CTD-velocity shows a clear peak around 0.1  
200 cps, short for cycles per s, which correspond to a period of 10 s. Such a peak is absent in both  
201 spectra of temperature T and density anomaly referenced to the surface  $\sigma_\theta$ . The correlation  
202 between  $dp/dt$  and T is not significantly different from zero (Fig. 2d,e). With conventional  
203 tubing and tube-ends, the surface wave variations would show in such  $\Delta T$ -graph (van Haren

204 and Laan, 2016). Without the effects of ship motions, considerably less corrections need to be  
205 applied for turbulence calculations (see below).

206

## 207 **2.2 Ocean turbulence calculation**

208 Turbulence is quantified using the analysis method by Thorpe (1977) on density ( $\rho$ )  
209 inversions of less dense water below a layer of denser water in a vertical ( $z$ ) profile. Such  
210 inversions are interpreted as turbulent overturns of mechanical energy mixing. Vertical  
211 turbulent kinetic energy dissipation rate ( $\varepsilon$ ) is a measure of the amount of kinetic energy put in  
212 a system for turbulent mixing. It is proportional to turbulent diapycnal flux (of density)  $K_z d\rho/dz$ .  
213 In practice it is determined by calculating overturning scales with magnitude  $|d|$ , just like  
214 turbulent eddy diffusivity ( $K_z$ ). The vertical density stratification is indicated by  $d\rho/dz$ . The  
215 turbulent overturning scales are obtained after reordering the potential density profile  $\sigma_\theta(z)$ ,  
216 which may contain inversions, into a stable monotonic profile  $\sigma_\theta(z_s)$  without inversions  
217 (Thorpe, 1977). After comparing raw and reordered profiles, displacements  $d = \min(|z-$   
218  $z_s|) \cdot \text{sgn}(z-z_s)$  are calculated that generate the stable profile. Then,

$$219 \quad \varepsilon = 0.64d^2N^3 \quad [\text{m}^2\text{s}^{-3}], \quad (1)$$

220 where  $N = \{-g/\rho(d\rho/dz + g\rho/c_s^2)\}^{1/2}$  (e.g., Gill, 1982) denotes the buoyancy frequency ( $\sim$  square-  
221 root of stratification as is clear from the equation) computed from the reordered profile. Here,  
222  $g$  is the acceleration of gravity and  $c_s$  the speed of sound reflecting pressure-compressibility  
223 effects.  $N$  is computed over a typical vertical length-scale of  $\Delta z = 100$  m, which more or less  
224 represents the scale of large internal waves that are supported by the density stratification. The  
225 numerical constant of 0.64 in (1) follows from empirically relating the overturning scale  
226 magnitude with the Ozmidov scale  $L_O$  of largest possible turbulent overturn in a stratified flow:  
227  $(L_O/|d|)_{\text{rms}} = 0.8$  (Dillon, 1982), a mean coefficient value from many realizations. Using  $K_z =$   
228  $\Gamma\varepsilon N^{-2}$  and a mean mixing efficiency coefficient of  $\Gamma = 0.2$  for the conversion of kinetic into  
229 potential energy for ocean observations that are suitably averaged over all relevant turbulent  
230 overturning scales of the mix of shear-, current differences, and convective, buoyancy driven,



231 turbulent overturning in large Reynolds number flow conditions (e.g., Osborn, 1980; Oakey,  
232 1982; Ferron et al., 1998; Gregg et al., 2018), we find,

$$233 \quad K_z = 0.128d^2N \quad [\text{m}^2\text{s}^{-1}]. \quad (2)$$

234 This parametrization is also valid for the upper ocean, as has been shown extensively by Oakey  
235 (1982) and recently confirmed by Gregg et al. (2019). The inference is that the upper ocean  
236 may be weakly stratified at times, but stratification and turbulence vary considerably with time  
237 and space. Sufficient averaging collapses coefficients to the mean values given above. This is  
238 confirmed in recent numerical modeling by Portwood et al. (2019).

239 As  $K_z$  is a mechanical turbulence coefficient it is not property-dependent like a molecular  
240 diffusion coefficient that is about 100-fold different for temperature compared to salinity.  $K_z$  is  
241 thus the same for all turbulent transport calculations no matter what gradient of what property.  
242 For example, the vertical turbulent flux of dissolved iron is computed as  $K_z d(\text{DFe})/dz$ .

243 According to Thorpe (1977), results from (1) and (2) are only useful after averaging over  
244 the size of a turbulent overturn instead of using single displacements. Here, root-mean-square-  
245 displacement values  $d_{\text{rms}}$  are not determined over individual overturns, as in Dillon (1982), but  
246 over 7 m vertical intervals (equivalent to about 200 raw data samples) that just exceed average  
247  $L_o$ . This avoids the complex distinction of smaller overturns in larger ones and allows the use  
248 of a single length scale of averaging. As a criterion for determining overturns we only used  
249 those data of which the absolute value of difference with the local reordered value exceeds a  
250 threshold of  $7 \times 10^{-5} \text{ kg m}^{-3}$ , which corresponds to applying a threshold of  $1.4 \times 10^{-3} \text{ kg m}^{-3}$  to raw  
251 data variations (e.g., Galbraith and Kelley, 1996; Stansfield et al., 2001; Gargett and Garner,  
252 2008). Vertically averaged turbulence values, short for averaged  $\epsilon$ - and  $K_z$ -values from (1) and  
253 (2), can be calculated to within an error of a factor of two to three, approximately. As will be  
254 demonstrated below, this is considerably less spread in values than the natural turbulence values  
255 variability over typically four orders of magnitude at a given position and depth in the ocean  
256 (e.g., Gregg, 1989).

257

### 258 **3 Results**

### 259 3.1 Physical parameters

260 An early morning vertical profile of density anomaly in the upper 500 m at a northern  
261 station (Fig. 3a) is characterized by a near-homogeneous layer of about 15 to 40 m, which is  
262 above a layer of relatively strong stratification and a smooth moderate stratification deeper  
263 below. In the near-homogeneous upper layer, in this example  $z > -30$  m, relatively large  
264 turbulent overturn displacements can be found of  $d = \pm 20$  m (Fig. 3b): so called large density  
265 inversions. For  $-200 < z < -30$  m, large turbulent overturns are few and far between. Turbulence  
266 dissipation rate (Fig. 3c) and eddy diffusivity (Fig. 3d) are characterized by relatively small  
267 displacement sizes of less than 5 m. For  $z < -200$  m, displacement values weakly increase with  
268 depth, together with stratification ( $\sim N^2$ ; Fig. 3e). Between  $-30 < z < 0$  m, turbulence dissipation  
269 rate values between  $< 10^{-11}$  and  $> 10^{-8} \text{ m}^2 \text{ s}^{-3}$  are similar to those found by others, using  
270 microstructure profilers (e.g., Oakey, 1982; Gregg, 1989), lowered acoustic Doppler current  
271 profiler or CTD-Thorpe scale analysis (e.g., Ferron et al., 1998; Walter et al., 2005; Kunze et  
272 al., 2006). Here, eddy diffusivities are found between  $< 10^{-5}$  and  $3 \times 10^{-3} \text{ m}^2 \text{ s}^{-1}$  and these values  
273 compare with previous near-surface results (Denman and Gargett, 1983). The relatively small  
274  $|d| < 5$  m displacements (Fig. 3b) are genuine turbulent overturns, and they resemble ‘Rankine  
275 vortices’, a common model of cyclones (van Haren and Gostiaux, 2014), as may be best visible  
276 in this example in the large turbulent overturn near the surface. The occasional erratic  
277 appearance in individual profiles, sometimes still visible in the ten-profile means, reflects  
278 smaller overturns in larger ones.

279 A mid-morning profile at a southern station shows different characteristics (Fig. 4),  
280 although 500 m vertically averaged turbulence values are similar to within 10% of those of the  
281 northern station. This 10% variation is well within the error bounds of about a factor of two. At  
282 this southern station, the near-surface layer is stably stratifying (Fig. 4a) and displays few  
283 overturning displacements (Fig. 4b), while the interior demonstrates rarer but occasional  
284 intense turbulent overturning (at  $z = -160$  m in Fig. 4), presumably due to internal wave  
285 breaking. At greater depths, stratification ( $\sim N^2$ ; Fig. 4e) weakly decreases, together with  $\epsilon$  (Fig.  
286 4c) and  $K_z$  (Fig. 4d).

287        Latitudinal overviews are given in Fig. 5 for: Average values over the upper  $z > -15$  m,  
288        which covers the diurnal mainly convective turbulent mixing range from the surface, average  
289        values between  $-100 < z < -25$  m, which covers the seasonal strong stratification, and average  
290        values between  $-500 < z < -100$  m, which covers the more permanent moderate stratification.  
291        Noting that all panels have a vertical axis representing a logarithmic scale, variations over  
292        nearly four orders of magnitude in turbulence dissipation rate (Fig. 5a) and eddy diffusivity  
293        (Fig. 5b) are observed between casts at the same station. This variation in magnitude is typically  
294        found in near-surface open-ocean turbulence microstructure profiles (e.g., Oakey, 1982). Still,  
295        considerable variability over about two orders of magnitude is observed between the averages  
296        from the different stations. This variation in station- and vertical averages far exceeds the  
297        instrumental error bounds of a factor of two (0.3 on a log-scale), and thus reveals local  
298        variability. The turbulence processes occur ‘intermittently’.

299        The observed variability over two orders of magnitude between yoyo-casts at a single  
300        station may be due to active convective overturning during early morning in the near-  
301        homogeneous upper layer, or due to internal wave breaking and sub-mesoscale variability  
302        deeper down. Despite the large variability at stations, trends are visible between stations in the  
303        upper 100 m over the  $32^\circ$  latitudinal range going poleward: Buoyancy frequency ( $\sim$  square root  
304        of stratification) steadily decreases significantly (p-value  $< 0.05$ ) given the spread of values at  
305        given stations, while turbulence values vary insignificantly with latitude as they remain the  
306        same or weakly increase by about half an order of magnitude (about a factor of 3). At a given  
307        depth range, turbulence dissipation rate roughly follow a log-normal distribution with standard  
308        deviations well exceeding half an order of magnitude. The comparison of latitudinal variations  
309        with the (log-normal) distribution are declared insignificant with  $p > 0.05$  when the mean values  
310        are found within 2 standard deviations (see Appendix A2). This is not only performed for  
311        turbulence dissipation rate, but also for other quantities. The trends suggest only marginally  
312        larger turbulence going poleward, which is possibly due to larger cooling from above and larger  
313        internal wave breaking deeper down. It is noted that the results are somewhat biased by the  
314        sampling scheme, which changed from 3 to 4 h after sunrise sampling at high latitudes to 4 to

315 5 h after sunrise sampling at lower latitudes, see the sampling hours after local sunrise in (Fig.  
316 5d). Its effect is difficult to quantify, but should not show up in turbulence values from deeper  
317 down ( $-500 < z < -100$  m).

318 Between  $-500 < z < -100$  m, no clear significant trend with latitude is visible in the  
319 turbulence values (Fig. 5a,b), although  $[K_z]$  weakly increases with increasing latitude at all  
320 levels between  $-500 < z < 0$  m, while buoyancy frequency significantly decreases (Fig. 5c). The  
321 data from well-stratified waters deeper down thus show the same latitudinal trend as the  
322 observations from the near-surface layers. Our turbulence values from CTD-data also confirm  
323 previous results by Jurado et al. (2012) who made microstructure profiler observations from the  
324 upper  $z > -100$  m along the same transect. Their results showed turbulence values remain  
325 unchanged over  $30^\circ$  latitude or increase by at most one order of magnitude, depending on depth  
326 level. Their ‘mixed’ layer ( $z \gtrsim -25$  m) turbulence values are similar to our  $z > -15$  m values  
327 and half to one order of magnitude larger than the present deeper observations. The slight  
328 discrepancy in values averaged over  $z > -25$  m may point at either i) a low bias due to a too  
329 strict criterion of accepting density variations for reordering applied here, or ii) a high bias of  
330 the  $\sim 10$ -m largest overturns having similar velocity scales (of about  $0.05 \text{ m s}^{-1}$ ) as their  $0.1 \text{ m}$   
331  $\text{s}^{-1}$  slowly descending SCAMP microstructure profiler. At greater depths,  $-500 < z < -100$  m, it  
332 is seen in the present observations that the spread in turbulence values over four orders of  
333 magnitude at a particular station is also large. This spread in values suggests that dominant  
334 turbulence processes show similar intermittency in weakly (at high-latitudes  $N \approx 10^{-2.5} \text{ s}^{-1}$ ) and  
335 moderately (at mid-latitudes  $N \approx 10^{-2.2} \text{ s}^{-1}$ ) stratified waters, respectively, for given resolution  
336 of the instrumentation.

337 Mean values of  $N$  are larger by half an order of magnitude in the seasonal pycnocline than  
338 those near the surface and in the more permanent stratification below (Fig. 5). Such local  
339 vertical variations in  $N$  have the same range of variation as observed horizontally across  
340 latitudes  $[30, 63.2]^\circ$  per depth level.

341

### 342 **3.2 Nutrient distributions and fluxes**

343 Vertical profiles of macro-nutrients generally resemble those of density anomaly in the  
344 upper  $z > -500$  m (Fig. 6). In the south, low macro-nutrient values are generally distributed over  
345 a somewhat larger near-surface mixed layer. The mixed layer depth, defined as the depth at  
346 which the temperature difference with respect to the surface was  $0.5^{\circ}\text{C}$  (Jurado et al., 2012),  
347 varies between about 20 and 30 m on the southern end of the transect and weakly becomes  
348 shallower with latitude (Fig. 7a). This weak trend may be expected from the summertime wind  
349 conditions that also barely vary with latitude (Fig. 7b,c). In contrast, the euphotic zone, defined  
350 as the depth of the 0.1% irradiance penetration level (Mojica et al., 2015), demonstrates a clear  
351 latitudinal trend decreasing from about 150 to 50 m (Fig. 7a). For  $z < -100$  m below the seasonal  
352 stratification, vertical gradients of macro-nutrients are large (Fig. 6b-d). Macro-nutrient values  
353 become more or less independent of latitude at depths below  $z < -500$  m. Dissolved iron profiles  
354 differ from macro-nutrient profiles, notably in the upper layer near the surface (Fig. 6a). At  
355 some southern stations, dissolved iron and to a lesser extent also phosphate, have relatively  
356 high concentrations closest to the surface. These near-surface concentration increases suggest  
357 atmospheric sources, most likely Saharan dust deposition (e.g., Rijkenberg et al., 2012).

358 As a function of latitude in the near-surface ‘mixed’ layer (Fig. 8), the vertical turbulent  
359 fluxes of dissolved iron and phosphate (representing the macro-nutrients, for graphical reasons,  
360 see the similarity in profiles in Fig.6b-d) are found constant or insignificantly ( $p > 0.05$ )  
361 increasing (Fig. 8d). Here, the mean eddy diffusivity values for the near-surface layer as  
362 presented in Fig. 5 are used for computing the fluxes. It is noted that in this layer turbulent  
363 overturning (Figs 3b, 4b) is larger and nutrients are mainly depleted (Fig. 6), except when  
364 replenished from atmospheric sources. Hereby, lateral diffusion is not considered important.  
365 More interestingly, the vertical turbulent fluxes of nutrients across the seasonal pycnocline (Fig.  
366 9) are found ambiguous or statistically independently varying with latitude (Fig. 9d). Likewise,  
367 the vertical turbulent fluxes of dissolved iron and phosphate are marginally constant with  
368 latitude across the more permanent stratification (Fig. 10). Nitrate fluxes show the same  
369 latitudinal trend, with values around  $10^{-6}$  mmol  $\text{m}^{-2}$   $\text{s}^{-1}$ . ~~Such values are of the same order of~~  
370 ~~magnitude as reported for the interior of the Saint Lawrence seaway (Cyr et al., 2015).~~ Overall,

371 the vertical turbulent nutrient fluxes across the seasonal and more permanent stratification  
372 resemble those of the physical vertical turbulent mass flux, which is equivalent to the  
373 distribution of turbulence dissipation rate and which is latitude-invariant (Fig. 5a).

374

#### 375 **4 Discussion**

376 Practically, the upright positioning CTD while using an adaptation consisting of a custom-  
377 made equal-surface inlet worked well to minimize ship-motion effects on variable flow-  
378 imposed temperature variations. This improved calculated turbulence values from CTD-  
379 observations in general and in near-homogeneous layers in particular. The indirect comparison  
380 with previous microstructure profiler observations along the same transect (Jurado et al., 2012)  
381 confirms the same trends, although occasionally turbulence values were lower (to one order of  
382 magnitude in the present study). This difference in values may be due to the time lapse of 8  
383 years between the observations, but more likely it is due to inaccuracies in one or both methods.  
384 It is noted that any ocean turbulence observations cannot be made better than to within a factor  
385 of two (Oakey, pers. comm.). In that respect, the standard CTD with the here presented  
386 adaptation is a cheaper solution than additional microstructure profiler observations. Although  
387 the general understanding, mainly amongst modellers, is that the Thorpe length method  
388 overestimates diffusivity (e.g., Scotti, 2015; Mater and Venayagamoorthy, 2015), this view is  
389 not shared amongst ocean observers (e.g., Gregg et al., 2018). In the large parameter space of  
390 the high Reynolds number environment of the ocean, turbulence properties vary constantly,  
391 with an interminglement of convection and shear-induced turbulence at various levels. Given  
392 sufficient averaging, and adequate mean value parametrization, the Thorpe length method is  
393 not observed to overestimate diffusivity. This property of adequate and sufficient averaging  
394 yields similar mean parameter values in recent modelling results estimating a mixing coefficient  
395 near the classical bound of 0.2 in stationary flows for a wide range of conditions (Portwood et  
396 al., 2019). It is noted that diffusivity always requires knowledge of stratification to obtain a  
397 turbulent flux, and it is better to consider turbulence dissipation rate for intercomparison

398 purposes. Nevertheless, future research may perform a more extensive comparison between  
399 Thorpe scale analysis data and deeper microstructure profiler data.

400 While our turbulence values are roughly similar to those of others transecting the NE-  
401 Atlantic over the entire water depth (Walter et al., 2005; Kunze et al., 2006), the focus in the  
402 present paper is on the upper 500 m because of its importance for upper-ocean marine biology.  
403 Our study demonstrates a significant decrease of stratification with increasing latitude and  
404 decreasing temperature that, however, does not lead to significant variation in turbulence values  
405 and vertical turbulent fluxes. Our direct estimates of the turbulent flux of nitrate into the  
406 euphotic zone are one to two orders of magnitude less than the rate of nitrate uptake within it  
407 for the same period. The turbulent flux of nitrate values are of the same order of magnitude as  
408 reported by others (Cyr et al., 2015 and references therein). In particular, the Martin et al. (2010)  
409 study in the Northeast Atlantic Ocean (at 49°N, 16°W) reported similar vertical nutrient fluxes  
410 during summer, which provides confidence in the methods used. The same authors reported  
411 that the vertical nitrate flux into the euphotic zone was much lower than the rate of nitrate  
412 uptake at the time. To determine these nitrate uptake rates, they spiked water samples were  
413 spiked with a minimum of 0.5 μM nitrate, representing ~10% of the ambient nitrate  
414 concentration. In our study area, the ambient nitrate concentrations in the euphotic zone were  
415 much lower (see also Mojica et al., 2015), implying a higher relative importance of nitrate input  
416 to the overall uptake demand. Still, primary productivity in the oligotrophic euphotic zone, as  
417 well as in the high latitude Atlantic, is mainly fueled by recycling (e.g., Gaul et al., 1999;  
418 Achterberg et al., 2020) and the supply of new nutrients by turbulent fluxes, however small,  
419 provides a welcome addition. Besides nutrient input resulting from vertical turbulent fluxes, is  
420 there is a role for latitudinal differences through the supply of nutrients by deep mixing events,  
421 and depending on the location, also potential upwelling and lateral transport events. These  
422 findings can suggest that global warming may not necessarily lead to a change in vertical  
423 turbulent exchange.

Formatted: Justified, Indent: First line: 0.2"

424 We ~~hypothesize~~ suggests that internal waves may drive the feed-back mechanism,  
425 participating in the subtle balance between destabilizing shear and stable (re)stratification ~~as~~  
426 outlined below.

427 Molecular diffusivity of heat is about  $10^{-7} \text{ m}^2 \text{ s}^{-1}$  in seawater, and nearly always smaller than  
428 turbulent diffusivity in the ocean. The average values of  $K_z$  during our study were typically 100  
429 to 1000 times larger than molecular diffusivity, which implies turbulent diapycnal mixing  
430 drives vertical fluxes despite the relatively slow turbulence compared to surface wave breaking.  
431 Depending on the gradient of a substance like nutrients or matter, the relatively slow turbulence  
432 may not necessarily provide weak fluxes  $K_z d(\text{substance})/dz$  into the photic zone. In the central  
433 North Sea, a relatively low mean value of  $K_z = 2 \times 10^{-5} \text{ m}^2 \text{ s}^{-1}$  comparable to values over the  
434 seasonal pycnocline here, was found sufficient to supply nutrients across the strong summer  
435 pycnocline to sustain the entire late-summer phytoplankton bloom in near-surface waters and  
436 to warm up the near-bottom waters by some  $3^\circ\text{C}$  over the period of seasonal stratification (van  
437 Haren et al., 1999). There, the turbulent exchange was driven by a combination of tidal currents  
438 modified by the stratification, shear by inertial motions driven by the Coriolis force (inertial  
439 shear) and internal wave breaking. Such drivers are also known to occur in the open ocean,  
440 although to unknown extent.

441 The here observed (lack of) latitudinal trends of  $\varepsilon$ ,  $K_z$  and  $N$  yield more or less the same  
442 information as the vertical trends in these parameters at all stations. In the vertical for  $z < -200$   
443 m, turbulence values of  $\varepsilon$  and  $K_z$  weakly vary with stratification. This is perhaps unexpected  
444 and contrary to the common belief of stratification hampering vertical turbulent exchange of  
445 matter including nutrients. It is less surprising when considering that increasing stratification is  
446 able to support larger shear. Known sources of destabilizing shear include near-inertial internal  
447 waves of which the vertical length-scale is relatively small compared to other internal waves,  
448 including internal tides (LeBlond and Mysak, 1978).

449 The dominance of inertial shear over shear by internal tidal motions (internal tide shear),  
450 together with larger energy in the internal tidal waves, has been observed in the open-ocean,  
451 e.g. in the Irminger Sea around  $60^\circ\text{N}$  (van Haren, 2007). The frequent atmospheric disturbances



452 in that area generate inertial motions and dominant inertial shear. Internal tides have larger  
453 amplitudes but due to much larger length scales they generate weaker shear, than inertial  
454 motions. Small-scale internal waves near the buoyancy frequency are abundant and may break  
455 sparsely in the ocean interior outside regions of topographic influence. However, larger  
456 destabilizing shear requires larger stable stratification to attain a subtle balance of ‘constant’  
457 marginal stability (van Haren et al., 1999). Not only storms, but other geostrophic adjustments,  
458 such as frontal collapse, may generate inertial wave shear also at low latitudes (Alford and  
459 Gregg, 2001), so that overall latitudinal dependence may be negligible. If shear-induced  
460 turbulence in the upper ocean is dominant it may thus be latitudinally independent (shallow  
461 observations by Jurado et al., 2012; deeper observations in present study). There are no  
462 indications that the overall open ocean internal wave field and (sub)mesoscale activities are  
463 energetically much different across the mid-latitudes. If internal tide sources would have been  
464 noticeable in dominated occurred right during our observations near the surface, they should  
465 have definitely given different results of clear differences in turbulence dissipation rates would  
466 have been found at our station near 48xxx °N (the latitude of near the Porcupine Bank), for  
467 example, compared with those at other stations.

468 Summarizing, our data imply study infers that vertical nutrient fluxes did not vary  
469 significantly with latitude and stratification, and thus This suggests that potential predicted  
470 changes in the physical environment like due to global ocean warming have little effect on  
471 vertical turbulent exchange. Supposing that enhanced warming leads to more stable  
472 stratification, such stratification can support more internal waves can be supported that can  
473 break (LeBlond and Mysak, 1978) (refs. ...), which upon breaking, can maintain the extent of  
474 vertical turbulent exchange and thereby maintaining the level of vertical turbulent exchange  
475 and thereby, for example, vertical nutrient fluxes. We thus hypothesize that, from a physical  
476 environment perspective, in stratified oligotrophic waters the nutrient availability input from  
477 deeper waters and corresponding summer phytoplankton productivity and growth are not  
478 expected to change (much) under with future environmental changes like global warming. We

Formatted: Indent: First line: 0.24"

479 invite future observations and numerical modelling to further investigate this suggestion and  
480 associated feed-back mechanisms such as internal wave breaking.

481

482 *Competing interests.* The authors declare that they have no conflict of interest.

483

484 *Acknowledgements.* We thank the master and crew of the R/V Pelagia for their pleasant  
485 contributions to the sea-operations. J. van Heerwaarden and R. Bakker made the CTD-  
486 modification.

487

APPENDIX A1

488

489 **Modification of CTD pump-tubing to minimize RAM-effects**

490 The unique pump system on SeaBird Electronics (SBE) CTDs, foremost on their high-  
491 precision full ocean depth shipborne and cable-lowered SBE911, minimizes the effects of flow  
492 variations (and inversions) past its T-C sensors (SeaBird, 2012). This reduction in flow  
493 variation is important, because the T-sensor has a slower response than the C-sensor. As data  
494 from the latter are highly temperature dependent, besides being pressure dependent, the precise  
495 matching of all three sensors is crucial for establishing proper salinity and density  
496 measurements, especially across rapid changes in any of the parameters. As flow past the T-  
497 sensor causes higher measurement values due to friction at the sensor tip, flow-fluctuations are  
498 to be avoided as they create artificial T-variations of about  $1 \text{ mK s m}^{-1}$  (Larson and Pedersen,  
499 1996).

500 However, while the pump itself is one thing, its tubing needs careful mounting as well, with  
501 in- and outlet at the same depth level (Sea-Bird, 2012). This is to prevent ram pressure  $P = \rho U^2$ ,  
502 for density  $\rho$  and flow speed  $U$ . Unfortunately, the SBE-manual shows tubing of different  
503 diameter, for in- and outlet. Different diameter tubing leads to velocity fluctuations of  $\pm 0.5 \text{ m}$   
504  $\text{s}^{-1}$  past the T-sensor, as was concluded from a simple experiment by van Haren and Laan  
505 (2016). The flow speed variations induce temperature variations of  $\pm 0.5 \text{ mK}$  and are mainly  
506 detectable in weakly stratified waters such as in the deep ocean, but also near the surface as  
507 observed in the present data. Using tubes of the same diameter opening remedied most of the  
508 effect, but only if the surface of the tube-opening is perpendicular to the main CT-motion as in  
509 a vertically mounted CTD. If it is parallel to the main motion as in a horizontally mounted CTD,  
510 the effect was found to be adverse. The make-shift onboard experiment in van Haren and Laan  
511 (2016) has now been cast into a better design (Fig. A1), of which the first results are presented  
512 in this paper.

APPENDIX A2

513

514 **PDFs of vertically averaged dissipation rate in comparison with latitudinal trends**

515 Ocean turbulence dissipation rate generally tends to a nearly log-normal distribution (e.g.,  
516 Pearson and Fox-Kemper, 2018), so that the probability density function (PDF) of the logarithm  
517 of  $\epsilon$ -values is normally distributed and can be described by the first two moments, the mean  
518 and its standard deviation. It is seen in Fig. A2a that the overall distribution of all present data  
519 indeed approaches lognormality, despite the relatively large length-scale used in the  
520 computations (cf., Yamazaki and Lueck, 1990). When the data are split in the three depth levels  
521 as in Fig. 5a, it is seen that  $\epsilon$  in the upper  $z > -15$  m layer is not log-normally distributed due to  
522 a few outlying high values confirming an ocean state dominated by a few turbulence bursts  
523 (Moum and Rippeth, 2009), whereas  $\epsilon$  in the deeper more stratified layers is nearly log-  
524 normally distributed.

525 When we compare the mean and standard deviations of the distributions with the extreme  
526 values of the latitudinal trends as computed for Fig. 5a it is seen that for none of the three depth  
527 levels the extreme values are found outside one standard deviation from the mean value. In fact,  
528 for deeper stratified waters the extreme values of the trends are found very close to the mean  
529 value. It is concluded that the mean dissipation rate does not show a significant trend with  
530 latitude, at all depth levels. The same exercise yields extreme buoyancy frequency values lying  
531 outside one standard deviation from the mean values for well-stratified waters, from which we  
532 conclude that stratification significantly decreases with latitude. This is inferable from Fig. 5c  
533 by investigating the spread of mean values around the trend line.

534

535 **References**

536 Alford, M. H. and Gregg, M. C.: Near-inertial mixing: Modulation of shear, strain and  
537 microstructure at low latitude, *J. Geophys. Res.*, 106, 16,947-16,968, 2001.

538 [Achterberg, E. P.: Trace element biogeochemistry in the high latitude North Atlantic Ocean:  
539 seasonal variations and volcanic inputs, \*Glob. Biogeochem. Cycl.\* in press, doi:  
540 \[10.1029/2020GB006674, 2020.\]\(#\)](#)

541 Charria, G., Theetten, S., Vandermeirsch, F., Yelekçi, Ö and Audiffren, N.: Interannual  
542 evolution of (sub)mesoscale dynamics in the Bay of Biscay, *Ocean Sci.*, 13, 777-797, 2017.

543 Cyr, F., Bourgault, D., Galbraith, P. S. and Gosselin, M.: Turbulent nitrate fluxes in the Lower  
544 St. Lawrence Estuary, Canada, *J. Geophys. Res.*, 120, 2308-2330,  
545 doi:10.1002/2014JC010272, 2015.

546 De Baar, H. J. W. et al.: Titan: A new facility for ultraclean sampling of trace elements and  
547 isotopes in the deep oceans in the international Geotraces program, *Mar. Chem.*, 111, 4-21,  
548 2008.

549 Denman, K. L. and Gargett, A. E.: Time and space scales of vertical mixing and advection of  
550 phytoplankton in the upper ocean, *Limnol. Oceanogr.*, 28, 801-815, 1983.

551 Dillon, T. M.: Vertical overturns: A comparison of Thorpe and Ozmidov length scales, *J.  
552 Geophys. Res.*, 87, 9601-9613, 1982.

553 Ferron, B., Mercier, H., Speer, K., Gargett, A. and Polzin, K.: Mixing in the Romanche Fracture  
554 Zone, *J. Phys. Oceanogr.*, 28, 1929-1945, 1998.

555 Galbraith, P. S. and Kelley, D. E.: Identifying overturns in CTD profiles, *J. Atmos. Oc.  
556 Technol.*, 13, 688-702, 1996.

557 Gargett, A. and Garner, T.: Determining Thorpe scales from ship-lowered CTD density  
558 profiles, *J. Atmos. Oc. Technol.*, 25, 1657-1670, 2008.

559 [Gaul, W., Antia, A. N. and Koeve, W.: Microzooplankton grazing and nitrogen supply of  
560 phytoplankton growth in the temperate and subtropical northeast Atlantic, \*Mar. Ecol. Progr.  
561 Ser.\*, 189, 93-104, 1999.](#)

562 Gill, A. E.: *Atmosphere-Ocean Dynamics*, Academic Press, Orlando, FL, USA, 662 pp, 1982.

563 Grasshoff, K., Kremling, K. and Ehrhardt, M.: Methods of seawater analysis, Verlag  
564 Chemie GmbH, Weinheim, 419 pp, 1983.

565 Gregg, M. C.: Scaling turbulent dissipation in the thermocline, J. Geophys. Res., 94, 9686-  
566 9698, 1989.

567 [Gregg, M. C., Sanford, T. B. and Winkel, D. P.: Reduced mixing from the breaking of internal](#)  
568 [waves in equatorial waters, Nature, 422, 513-515, 2003.](#)

569 Gregg, M. C., D'Asaro, E. A., Riley, J. J. and Kunze, E.: Mixing efficiency in the ocean, Ann.  
570 Rev. Mar. Sci., 10, 443-473, 2018.

571

572 [Henyey, F. S., Wright, J. and Flatte, S. M.: Energy and action flow through the internal wave](#)  
573 [field - an eikonal approach, J. Geophys. Res., 91, 8487-8495, 1986.](#)

574 Hernández-Hernández, N. et al.: Drivers of plankton distribution across mesoscale eddies at  
575 submesoscale range, Front. Mar. Sci., 7, 667, doi:10.3389/fmars.2020.00667, 2020.

576

577 [Hibiya T., Nagasawa, M. and Niwa, Y.: Latitudinal dependence of diapycnal diffusivity in the](#)  
578 [thermocline observed using a microstructure profiler, Geophys. Res. Lett., 34, L24602,](#)  
579 [2007.](#)

580 Huisman, J., Pham Thi, N. N., Karl, D. M. and Sommeijer, B.: Reduced mixing generates  
581 oscillations and chaos in the oceanic deep chlorophyll maximum, Nature, 439, 322-325,  
582 2006.

583 Jurado, E., van der Woerd, H. J. and Dijkstra, H. A.: Microstructure measurements along a  
584 quasi-meridional transect in the northeastern Atlantic Ocean, J. Geophys. Res., 117,  
585 C04016, doi:10.1029/2011JC07137, 2012.

586 IOC, SCOR, IAPSO: The international thermodynamic equation of seawater – 2010:  
587 Calculation and use of thermodynamic properties, Intergovernmental Oceanographic  
588 Commission, Manuals and Guides No. 56, UNESCO, Paris, France, 196 pp, 2010.

Formatted: Justified, Indent: Left: 0", Hanging: 0.25", Line spacing: Double

Formatted: Justified, Indent: Left: 0", Hanging: 0.25", Line spacing: Double

589 Johnson, K. S., Gordon, R. M. and Coale, K. H.: What controls dissolved iron concentrations  
590 in the world ocean? *Mar. Chem.*, 57, 137-161, 1997.

591 Klunder, M. B., Laan, P., Middag, R., De Baar, H. J. W. and van Ooijen, J. C.: Dissolved iron  
592 in the Southern Ocean (Atlantic sector), *Deep-Sea Res. II*, 58, 2678-2694, 2011.

593 Kunze, E., Firing, E., Hummon, J. M., Chereskin, T. K. and Thurnherr, A. M.: Global  
594 abyssal mixing inferred from lowered ADCP shear and CTD strain profiles, *J. Phys.*  
595 *Oceanogr.* 36, 1553-1576, 2006.

596 Larson, N., Pedersen, A. M.: Temperature measurements in flowing water: viscous heating  
597 of sensor tips, Proc. 1st IGHEM Meeting, Montreal, PQ, Canada. [Available online at  
598 [http://www.seabird.com/technical\\_references/viscous.htm](http://www.seabird.com/technical_references/viscous.htm)], 1996.

599 LeBlond, P. H. and Mysak, L. A.: *Waves in the Ocean*, Elsevier, Amsterdam NL, 602 pp, 1978.

600 Lueck, R. G.: Thermal inertia of conductivity cells: Theory, *J. Atmos. Oc. Technol.*, 7, 741-  
601 755, 1990.

602 Mater, B. D., Venayagamoorthy, S. K., St. Laurent, L. and Moum, J. N.: Biases in Thorpe-scale  
603 estimates of turbulence dissipation. Part I: Assessments from largescale overturns in  
604 oceanographic data, *J. Phys. Oceanogr.*, 45, 2497-2521, 2015.

605

606 [Martin A. P., et al.: The supply of nutrients due to vertical turbulent mixing: A study at the](#)  
607 [Porcupine abyssal plain study site in the northeast Atlantic, \*Deep-Sea Res. II\*, 57, 1293-](#)  
608 [1302, 2010.](#)

609 Mensah, V., Le Menn, M. and Morel, Y.: Thermal mass correction for the evaluation of salinity,  
610 *J. Atmos. Oc. Tech.*, 26, 665-672, 2009.

611 Middag, R., de Baar, H. J. W., Laan, P. and Bakker, K.: Dissolved aluminium and the silicon  
612 cycle in the Arctic Ocean, *Marine Chemistry*, 115, 176-195, 2009.

613 Mojica, K. D. A. et al.: Phytoplankton community structure in relation to vertical stratification  
614 along a north-south gradient in the Northeast Atlantic Ocean, *Limnol. Oceanogr.*, 60, 1498-  
615 1521, 2015.

616 Mojica, K. D. A., Huisman, J., Wilhelm, S. W. and Brussaard, C. P. D.: Latitudinal variation  
617 in virus-induced mortality of phytoplankton across the North Atlantic Ocean, *ISME J.*, 10,  
618 500-513, 2016.

619 Moum, J. N. and Rippeth, T. P.: Do observations adequately resolve the natural variability of  
620 oceanic turbulence?, *J. Mar. Sys.*, 77, 409-417, 2009.

621 Murphy, J. and Riley, J. P.: A modified single solution method for the determination of  
622 phosphate in natural waters, *Anal. Chim. Acta*, 27, 31-36, 1962.

623 Oakey, N. S.: Determination of the rate of dissipation of turbulent energy from simultaneous  
624 temperature and velocity shear microstructure measurements, *J. Phys. Oceanogr.*, 12, 256-  
625 271, 1982.

626 Osborn, T. R.: Estimates of the local rate of vertical diffusion from dissipation measurements,  
627 *J. Phys. Oceanogr.*, 10, 83-89, 1980.

628 Pearson, B. and Fox-Kemper, B.: Log-normal turbulence dissipation in global ocean models,  
629 *Phys. Rev. Lett.*, 120, 094501, 2018.

630 Portwood, G. D., de Bruyn Kops, S. M. and Caulfield, C. P.: Asymptotic dynamics of high  
631 dynamic range stratified turbulence, *Phys. Rev. Lett.*, 122, 194504, 2019.

632 Rijkenberg, M. J. A. et al.: Fluxes and distribution of dissolved iron in the eastern (sub-) tropical  
633 North Atlantic Ocean, *Glob. Biogeochem. Cycl.*, 26, GB3004,  
634 doi:10.1029/2011GB004264, 2012.

635 Rijkenberg, M. J. A. et al.: "PRISTINE", a new high volume sampler for ultraclean sampling  
636 of trace metals and isotopes, *Mar. Chem.*, 177, 501-509, 2015.

637 Sarmiento, J. L. et al.: Response of ocean ecosystems to climate warming, *Glob. Biogeochem.*  
638 *Cycl.*, 18, doi:10.1029/2003GB002134, 2004.

639 Scotti, A.: Biases in Thorpe-scale estimates of turbulence dissipation. Part II: energetics  
640 arguments and turbulence simulations, *J. Phys. Oceanogr.*, 45, 2522-2543, 2015.

641 Sea-Bird: Fundamentals of the TC duct and pump-controlled flow used on Sea-Bird CTDs,  
642 *Proc. Sea-Bird Electronics Appl. note 38*, SBE, Bellevue, WA, USA, 5 pp, 2012.



643 Smith, W. H. F. and Sandwell, D. T. : Global seafloor topography from satellite altimetry and  
644 ship depth soundings, *Science* 277, 1957-1962, 1997.

645 Stansfield, K., Garrett, C., Dewey, R.: The probability distribution of the Thorpe displacement  
646 within overturns in Juan de Fuca Strait, *J. Phys. Oceanogr.*, 31, 3421-3434, 2001.

647 Strickland, J. D. H. and Parsons, T. R.: A practical handbook of seawater analysis, First  
648 edition, Fisheries Research Board of Canada, Bulletin, 167, 293 pp, 1968.

649 Thorpe, S. A.: Turbulence and mixing in a Scottish loch, *Phil. Trans. Roy. Soc. Lond. A*, 286,  
650 125-181, 1977.

651

652 van Haren, H.: Tidal and near-inertial peak variations around the diurnal critical latitude,  
653 *Geophys. Res. Lett.*, 32, L23611, doi:10.1029/2005GL024160, 2005b.

654 van Haren, H.: Inertial and tidal shear variability above Reykjanes Ridge, *Deep-Sea Res. I*, 54,  
655 856-870, 2007.

656 van Haren, H. and Gostiaux, L.: Characterizing turbulent overturns in CTD-data, *Dyn. Atmos.*  
657 *Oc.*, 66, 58-76, 2014.

658 van Haren, H. and Laan, M.: An in-situ experiment identifying flow effects on temperature  
659 measurements using a pumped CTD in weakly stratified waters, *Deep-Sea Res. I*, 111, 11-  
660 15, 2016.

661 van Haren, H., Maas, L., Zimmerman, J. T. F., Ridderinkhof, H. and Malschaert, H.: Strong  
662 inertial currents and marginal internal wave stability in the central North Sea, *Geophys.*  
663 *Res. Lett.*, 26, 2993-2996, 1999.

664 Walter, M., Mertens, C. and Rhein, M.: Mixing estimates from a large-scale hydrographic  
665 survey in the North Atlantic, *Geophys. Res. Let.*, 32, L13605, doi:10.1029/2005GL022471,  
666 2005.

667 Yamazaki, H. and Lueck, R.: Why oceanic dissipation rates are not lognormal, *J. Phys.*  
668 *Oceanogr.*, 20, 1907-1918, 1990.

669

Formatted: Indent: Left: 0", First line: 0"

671 **Figure 1.** Bathymetry map of the Northeast Atlantic Ocean based on the 9.1 ETOPO-1 version  
672 of satellite altimetry-derived data by Smith and Sandwell (1997). The numbered circles  
673 indicate the CTD stations. Depth contours are at 2500 and 5000 m.

674

675 **Figure 2.** Test of effective removal of ship motions in CTD-data after pump in- and outlet  
676 modification. Nearly raw 24 Hz sampled downcast data obtained from northern station 32  
677 (cast 9). Short example time series for the 20-m depth range [10, 30] m. (a) Detrended  
678 pressure (blue) and its (negative signed) first time derivative  $-dp/dt$ , 2-dbar-smoothed  
679 (purple). (b) Detrended temperature. (c) Moderately smoothed ( $\sim 30$  degrees of freedom;  
680 dof) spectra of data from the 5 to 500 m depth range. (d) Moderately smoothed (40 dof)  
681 coherence between  $dp/dt$  and T from c., with dashed line indicating the 95% significance  
682 level. (e) Corresponding phase difference.

683

684 **Figure 3.** Upper 500 m of turbulence characteristics computed from downcast density anomaly  
685 data applying a threshold of  $7 \times 10^{-5} \text{ kg m}^{-3}$ . Northern station 29, cast 2. (a) Unordered, 'raw'  
686 profile of density anomaly referenced to the surface. (b) Overturn displacements following  
687 reordering of the profiles in a. Slopes  $\frac{1}{2}$  (solid lines) and 1 (dashed lines) are indicated. (c)  
688 Logarithm of dissipation rate computed from the profiles in a., averaged over 7 m intervals.  
689 (d) As c., but for eddy diffusivity. (e) Logarithm of buoyancy frequency computed after  
690 reordering the profiles of a.

691

692 **Figure 4.** As Fig. 3, but for a southern station. Upper 500 m of turbulence characteristics  
693 computed from downcast density anomaly data applying a threshold of  $7 \times 10^{-5} \text{ kg m}^{-3}$ .  
694 Southern station 3, cast 4. (a) Unordered, 'raw' profile of density anomaly referenced to  
695 the surface. (b) Overturn displacements following reordering of the profiles in a. Slopes  $\frac{1}{2}$   
696 (solid lines) and 1 (dashed lines) are indicated. (c) Logarithm of dissipation rate computed  
697 from the profiles in a., averaged over 7 m intervals. (d) As c., but for eddy diffusivity. (e)  
698 Logarithm of buoyancy frequency computed after reordering the profiles of a.

699

700 **Figure 5.** Summer 2017 latitudinal transect along  $17\pm 5^\circ\text{W}$  of turbulence values for upper 15 m  
701 averages (green) and averages between  $-100 < z < -25$  m (blue, seasonal pycnocline) and -  
702  $500 < z < -100$  m (black, more permanent pycnocline) from short yoyos of 3 to 6 CTD-  
703 casts. Values are given per cast (o) and station average (heavy circle with x; the size  
704 corresponds with  $\pm$ the standard error for turbulence parameters). (a) Logarithm of  
705 dissipation rate. (b) Logarithm of diffusivity. (c) Logarithm of buoyancy frequency (the  
706 small symbols have the size of  $\pm$ the standard error). (d) Hour of sampling after sunrise.

707

708 **Figure 6.** Upper 500 m profiles for stations at three latitudes. (a) Density anomaly referenced  
709 to the surface, including profiles from Fig. 3a and 4a. (b) Nitrate plus nitrite. (c) Phosphate.  
710 (d) Silicate. (e) Dissolved iron.

711

712 **Figure 7.** Latitudinal transect of near-surface layers and wind conditions measured at stations  
713 during the observational survey. (a) Mixed layer depth (x) and euphotic zone (o). (b) Wind  
714 speed. (c) Wind direction.

715

716 **Figure 8.** Latitudinal transect of near-surface nutrient concentrations. (a) Dissolved iron  
717 [measured at depths indicated](#). (b) Nitrate plus nitrite (red) and phosphate (blue, scale times  
718 10) [measured at depths indicated in a](#). (c) Logarithm of vertical gradients of values  
719 dissolved iron in a. ([o-red](#)) and phosphate in b. ([x-blue](#)). (d). Vertical turbulent fluxes of  
720 concentration [gradients](#) in c. using average surface  $K_z$  from Fig. 5b, [valid for depth average](#)  
721 [\(here, ~17 m\) of depths in a](#).

722

723 **Figure 9.** As Fig. 8, but for  $-100 < z < -25$  m, [with fluxes for ~62 m in d](#).

724

725 **Figure 10.** As Fig. 8, but for  $-600$  (few nutrients sampled at  $500 < z < -100$  m, [with fluxes for](#)  
726 [~350 m in d](#).

727

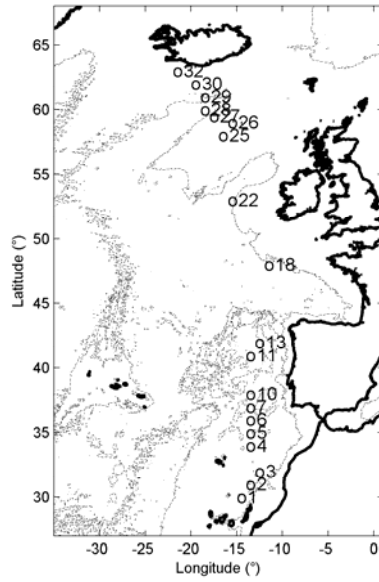
728 **Fig. A1.** SBE911 CTD-pump in- and outlet modification following the findings in van Haren  
729 and Laan (2016). (a) The T- and C-sensors clamped together with a structure holding in-  
730 and outlet pump-tubing of exactly the same diameter, separated at 0.3 m distance in the  
731 horizontal plane. (b) The modification of a. mounted in the CTD-frame.

732

733 **Fig. A2.** Probability Density Functions of logarithm of vertically averaged dissipation rate in  
734 comparison with latitudinal trend extreme values. (a) Distribution as a function of latitude  
735 for all data. (b) As a, but for the upper 15 m averages only. The mean value is given by the  
736 vertical purple line, with the horizontal line indicating +/- 1 standard deviation. The vertical  
737 light-blue lines indicate the best-fit value of the trend for 30° and 63°N. (c) As b, but for  
738 averages between  $-100 < z < -25$  m. (d) As c, but for averages between  $-500 < z < -100$  m.

739

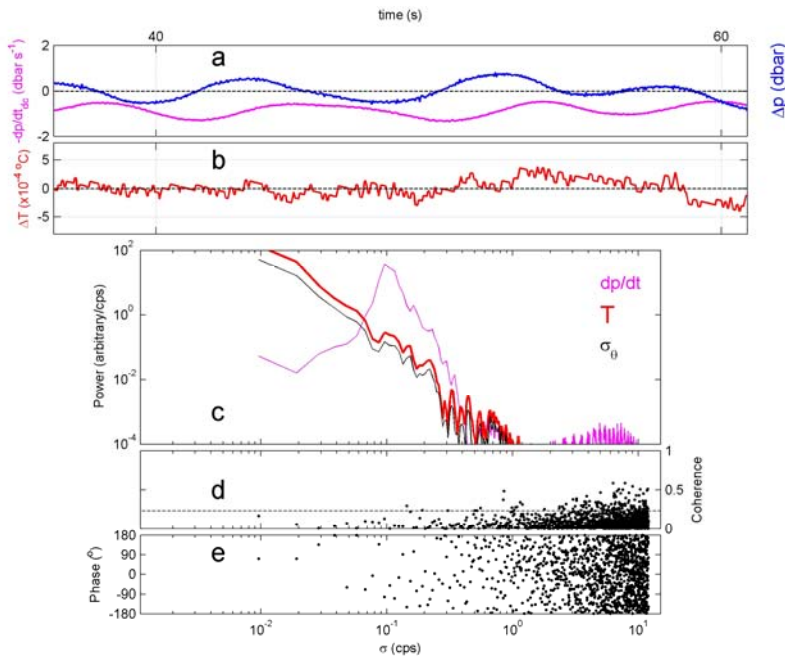
740



741  
 742  
 743  
 744  
 745

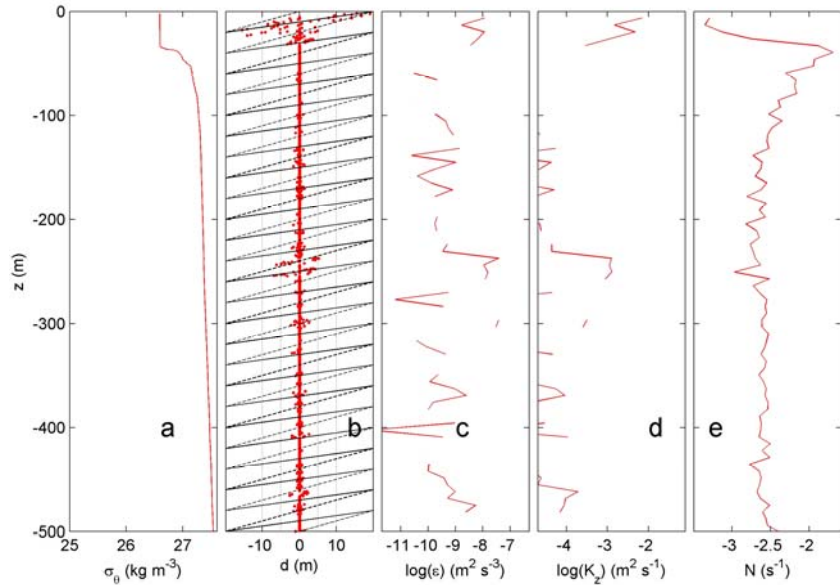
**Figure 1.** Bathymetry map of the Northeast Atlantic Ocean based on the 9.1 ETOPO-1 version of satellite altimetry-derived data by Smith and Sandwell (1997). The numbered circles indicate the CTD stations. Depth contours are at 2500 and 5000 m.

746



747  
748  
749  
750  
751  
752  
753  
754  
755  
756

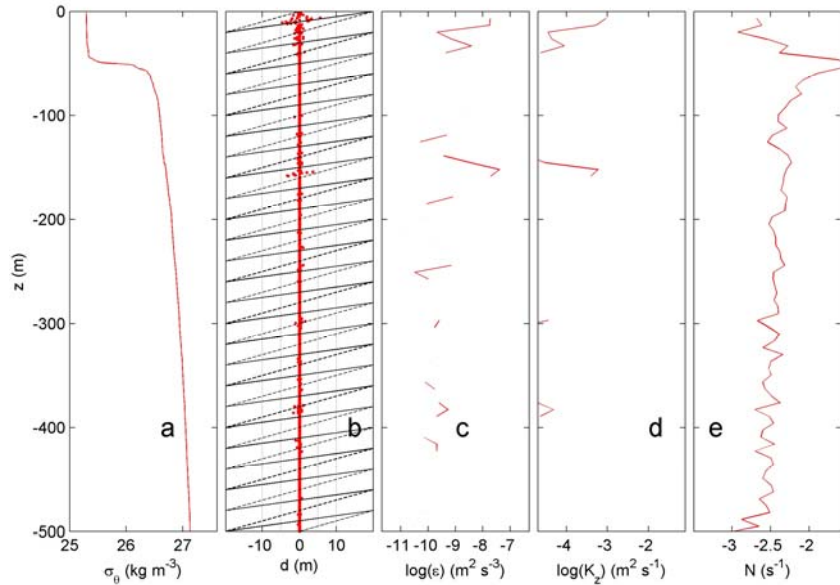
**Figure 2.** Test of effective removal of ship motions in CTD-data after pump in- and outlet modification. Nearly raw 24 Hz sampled downcast data obtained from northern station 32 (cast 9). Short example time series for the 20-m depth range [10, 30] m. (a) Detrended pressure (blue) and its (negative signed) first time derivative  $-dp/dt$ , 2-dbar-smoothed (purple). (b) Detrended temperature. (c) Moderately smoothed ( $\sim 30$  degrees of freedom; dof) spectra of data from the 5 to 500 m depth range. (d) Moderately smoothed (40 dof) coherence between  $dp/dt$  and  $T$  from c., with dashed line indicating the 95% significance level. (e) Corresponding phase difference.



757  
 758  
 759  
 760  
 761  
 762  
 763  
 764  
 765

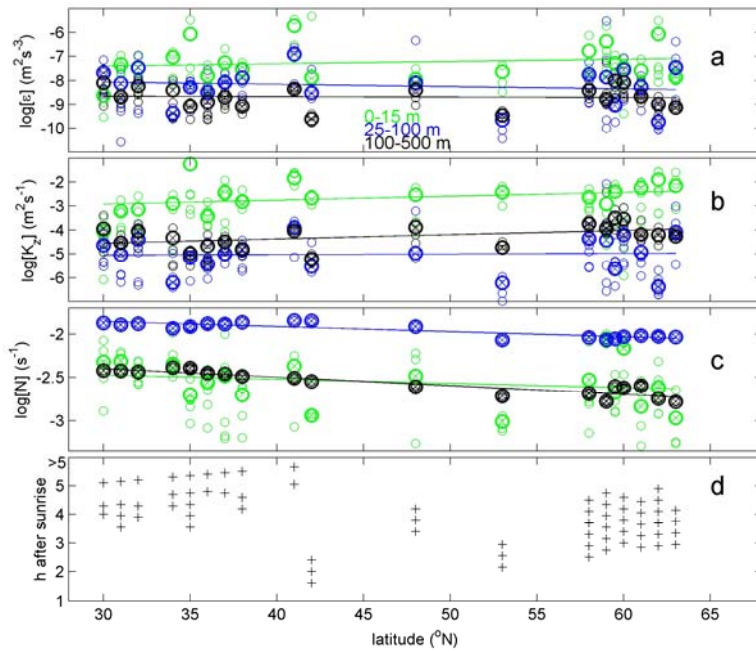
**Figure 3.** Upper 500 m of turbulence characteristics computed from downcast density anomaly data applying a threshold of  $7 \times 10^{-5} \text{ kg m}^{-3}$ . Northern station 29, cast 2. (a) Unordered, ‘raw’ profile of density anomaly referenced to the surface. (b) Overturn displacements following reordering of the profiles in a. Slopes  $\frac{1}{2}$  (solid lines) and 1 (dashed lines) are indicated. (c) Logarithm of dissipation rate computed from the profiles in a., averaged over 7 m intervals. (d) As c., but for eddy diffusivity. (e) Logarithm of buoyancy frequency computed after reordering the profiles of a.





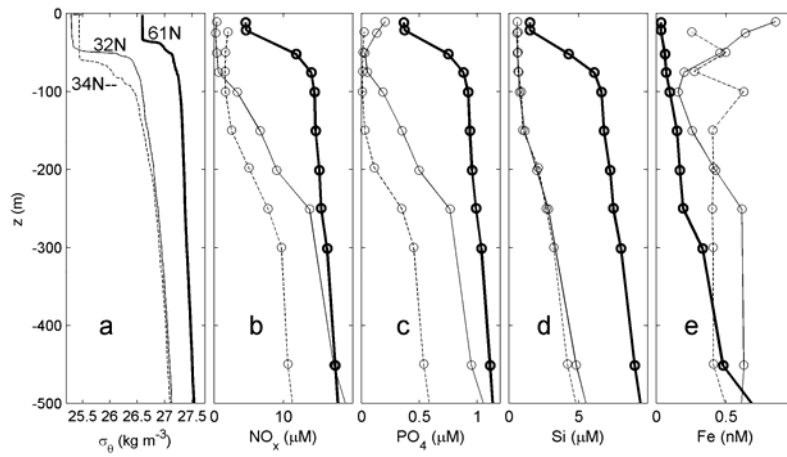
766  
 767  
 768  
 769  
 770  
 771  
 772  
 773  
 774

**Figure 4.** As Fig. 3, but for a southern station. Upper 500 m of turbulence characteristics computed from downcast density anomaly data applying a threshold of  $7 \times 10^{-5} \text{ kg m}^{-3}$ . Southern station 3, cast 4. (a) Unordered, ‘raw’ profile of density anomaly referenced to the surface. (b) Overturn displacements following reordering of the profiles in a. Slopes  $\frac{1}{2}$  (solid lines) and 1 (dashed lines) are indicated. (c) Logarithm of dissipation rate computed from the profiles in a., averaged over 7 m intervals. (d) As c., but for eddy diffusivity. (e) Logarithm of buoyancy frequency computed after reordering the profiles of a.



775  
 776  
 777  
 778  
 779  
 780  
 781  
 782  
 783

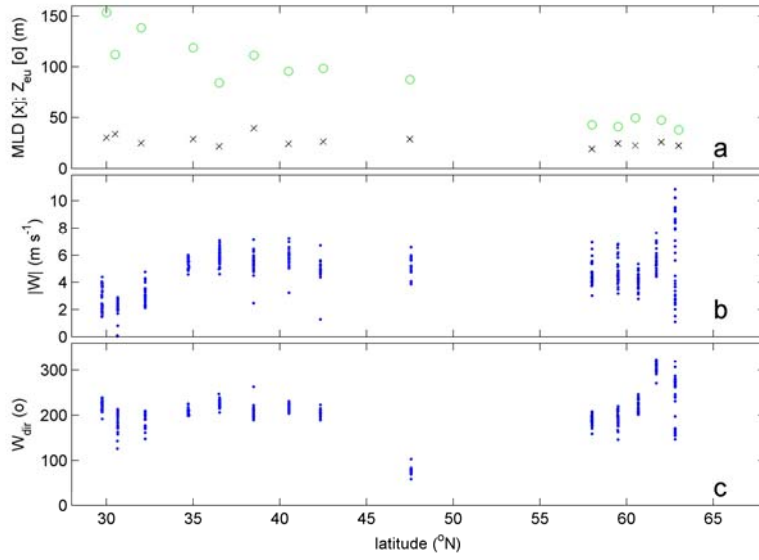
**Figure 5.** Summer 2017 latitudinal transect along  $17 \pm 5^\circ \text{W}$  of turbulence values for upper 15 m averages (green) and averages between  $-100 < z < -25$  m (blue, seasonal pycnocline) and  $-500 < z < -100$  m (black, more permanent pycnocline) from short yoyos of 3 to 6 CTD-casts. Values are given per cast (o) and station average (heavy circle with x; the size corresponds with  $\pm$ the standard error for turbulence parameters). (a) Logarithm of dissipation rate. (b) Logarithm of diffusivity. (c) Logarithm of buoyancy frequency (the small symbols have the size of  $\pm$ the standard error). (d) Hour of sampling after sunrise.



784  
 785  
 786  
 787  
 788

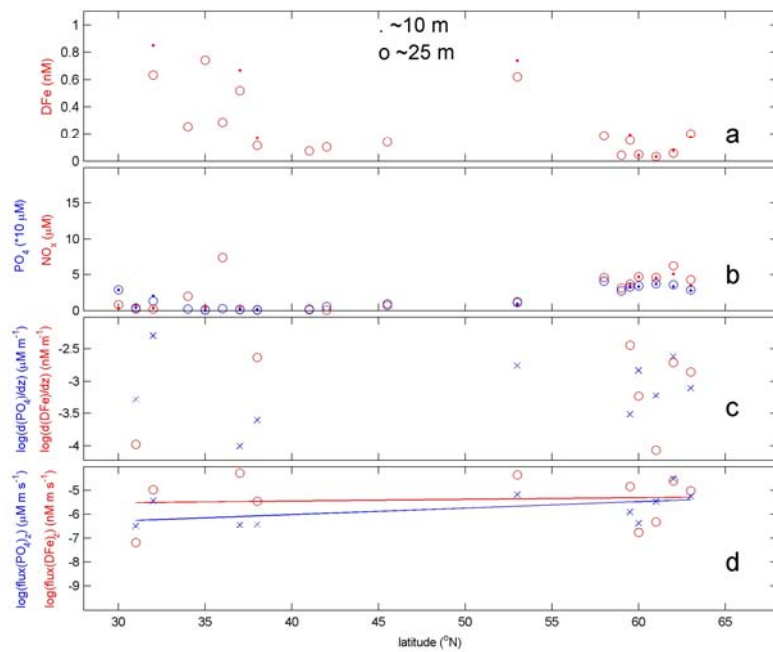
**Figure 6.** Upper 500 m profiles for stations at three latitudes. (a) Density anomaly referenced to the surface, including profiles from Fig. 3a and 4a. (b) Nitrate plus nitrite. (c) Phosphate. (d) Silicate. (e) Dissolved iron.

789



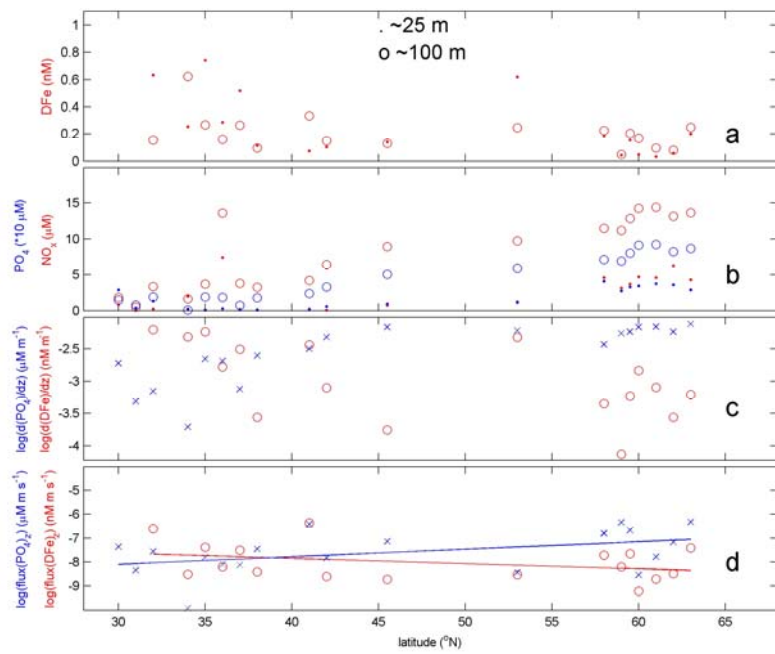
790  
791  
792  
793  
794

**Figure 7.** Latitudinal transect of near-surface layers and wind conditions measured at stations during the observational survey. (a) Mixed layer depth (x) and euphotic zone (o). (b) Wind speed. (c) Wind direction.



795  
796  
797  
798  
799  
800  
801  
802

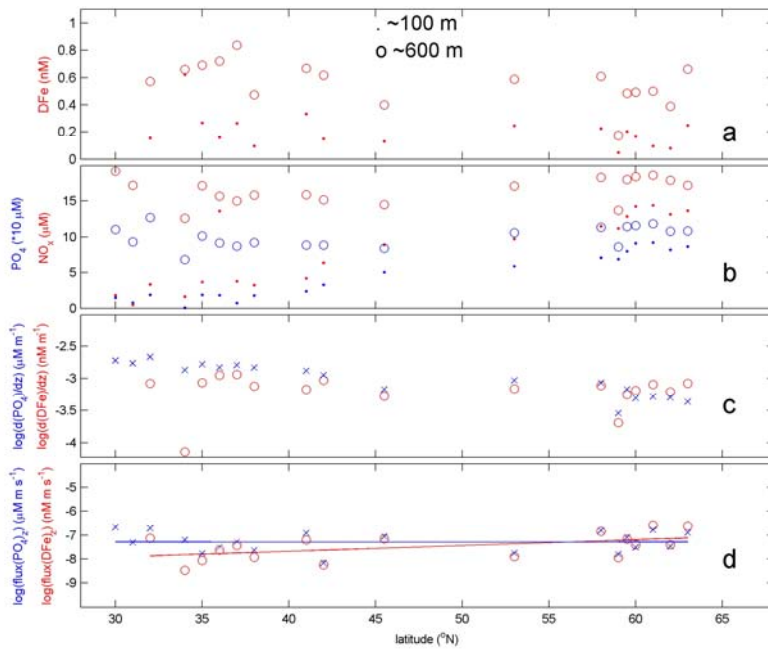
**Figure 8.** Latitudinal transect of near-surface nutrient concentrations. (a) Dissolved iron [measured at depths indicated](#). (b) Nitrate plus nitrite (red) and phosphate (blue, scale times 10) [measured at the depths indicated in a](#). (c) Logarithm of vertical gradients of values dissolved iron in a. [\(o-red\)](#) and phosphate in b. [\(x-blue\)](#). (d). Vertical turbulent fluxes of concentration [gradients](#) in c. using average surface  $K_z$  from Fig. 5**e**, [valid for the depth average \(here, ~17 m\) of depths in a](#).



803  
804  
805

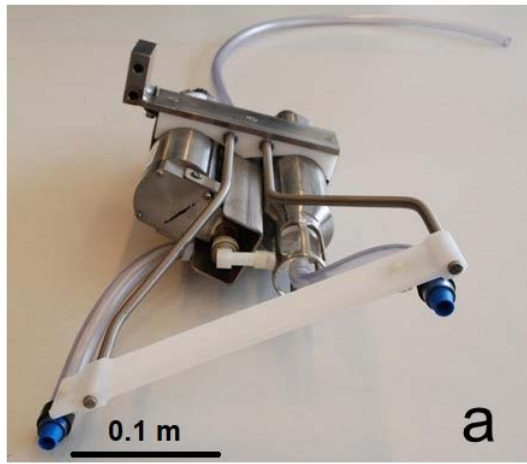
**Figure 9.** As Fig. 8, but for  $-100 < z < -25$  m, [with fluxes for ~62 m in d.](#)

806



807  
808  
809  
810

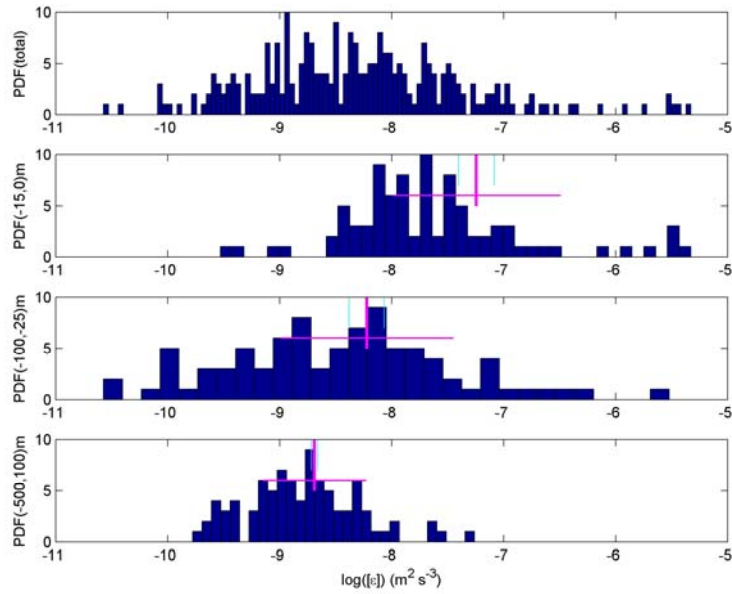
**Figure 10.** As Fig. 8, but for -600 (few nutrients sampled at 500)  $< z < -100$  m, [with fluxes for ~350 m in d.](#)



811  
812  
813  
814  
815  
816

**Fig. A1.** SBE911 CTD-pump in- and outlet modification following the findings in van Haren and Laan (2016). (a) The T- and C-sensors clamped together with a structure holding in- and outlet pump-tubing of exactly the same diameter, separated at 0.3 m distance in the horizontal plane. (b) The modification of a. mounted in the CTD-frame.





817  
 818  
 819  
 820  
 821  
 822  
 823  
 824  
 825  
 826

**Fig. A2.** Probability Density Functions of logarithm of vertically averaged dissipation rate in comparison with latitudinal trend extreme values. (a) Distribution as a function of latitude for all data. (b) As a, but for the upper 15 m averages only. The mean value is given by the vertical purple line, with the horizontal line indicating  $\pm 1$  standard deviation. The vertical light-blue lines indicate the best-fit value of the trend for  $30^\circ$  and  $63^\circ\text{N}$ . (c) As b, but for averages between  $-100 < z < -25$  m. (d) As c, but for averages between  $-500 < z < -100$  m.